Detached Eddy Simulation of the UH-60 Rotor Wake Using Adaptive Mesh Refinement

Neal M. Chaderjian
Research Scientist
Fundamental Modeling & Simulation Branch
Neal.Chaderjian@nasa.gov

Jasim U. Ahmad
Aerospace Engineer
Applied Modeling & Simulation Branch
Jasim.U.Ahmad@nasa.gov

NASA Ames Research Center, Moffett Field, CA, 94035

Time-dependent Navier-Stokes flow simulations have been carried out for a UH-60 rotor with simplified hub in forward flight and hover flight conditions. Flexible rotor blades and flight trim conditions are modeled and established by loosely coupling the OVERFLOW Computational Fluid Dynamics (CFD) code with the CAMRAD II helicopter comprehensive code. High order spatial differences, Adaptive Mesh Refinement (AMR), and Detached Eddy Simulation (DES) are used to obtain highly resolved vortex wakes, where the largest turbulent structures are captured. Special attention is directed towards ensuring the dual time accuracy is within the asymptotic range, and verifying the loose coupling convergence process using AMR. The AMR/DES simulation produced vortical worms for forward flight and hover conditions, similar to previous results obtained for the TRAM rotor in hover. AMR proved to be an efficient means to capture a rotor wake without apriori knowledge of the wake shape.

Nomenclature

a	Fluid speed of sound
A	Rotor disk area, πR^2
c	Local rotor blade chord length
c_t	Sectional blade thrust coefficient, $\frac{T'}{c\frac{1}{2}\rho(\Omega R)^2}$
c_{tip}	Rotor blade tip chord length
C_M	Rotor pitching moment coefficient, $\frac{M}{\frac{1}{2}\rho V_{tip}^2 A}$
C_N	Rotor normal force coefficient, $\frac{N}{\frac{1}{2}\rho V_{tip}^2 A}$
C_Q	Torque coefficient, $\frac{Q}{\rho(\Omega R)^2 RA}$
C_T	Thrust coefficient, $\frac{T}{\rho(\Omega R)^2 A}$
FM	Figure of merit, $\frac{C_T^{3/2}}{\sqrt{2}C_Q}$
M	Rotor pitching moment
M'	Sectional blade pitching moment
M_{tip}	Blade tip Mach number, $\frac{\Omega R}{a}$
M^2c_m	Sectional pitching moment coefficient, $\frac{M'}{\frac{1}{2}\rho a^2 c}$
M^2c_n	Sectional normal force coefficient, $\frac{N'}{\frac{1}{2}\rho a^2 c}$
N	Rotor normal force
N'	Sectional blade normal force
NB	Near body
N_i	Number of dual-time sub-iterations
OB	Off body
Q	Rotor torque
r	Radial position
R	Rotor radius
Re	Reynolds number, $\frac{V_{tip}c_{tip}}{\nu}$
T	Rotor thrust
T'	Sectional blade thrust
u,v,w	Cartesian velocity components
V	Velocity magnitude
x, y, z	Cartesian coordinates
y^+	Non-dimensional viscous wall spacing
β	Blade flap angle, deg
Δ	Grid spacing
Δt	Time step, deg rotation
δ	Boundary layer thickness
$\delta_X^{(6)}$	6th-order central difference operator
δ_{X^6}	6th-derivative artificial dissipation operator
ζ	Blade Lag angle, deg
θ	Blade collective pitch angle, deg
ν	Fluid kinematic viscosity
ν_t	Kinematic turbulent eddy viscosity
$\tilde{\nu}$	Turbulence variable
ρ	Fluid density
ψ	Azimuthal angle of rotor blade, deg
Ω	Rotor rotational speed or vorticity magnitude

Presented at the American Helicopter Society 68th Annual Forum, Fort Worth, TX, May 1-3, 2012. This is a work of the U.S. Government and is not subject to copyright protection in the U.S.

Introduction

The accurate simulation of rotorcraft flow fields with Computational Fluid Dynamics (CFD) continues to be a challenging problem. Unlike fixed-wing applications, a rotor blade can encounter the tip vortices of other blades, and in some cases its own tip vortex. This interaction can strongly affect the rotor-blade loads and performance, generate high levels of noise, and produce a strong interaction between the rotor blade trailing edge shear layers and the tip vortices. The situation is further complicated by flexible rotor blades, which require the coupling of fluids and structures solvers, and a trim algorithm for static flight conditions.

Chaderjian and Buning[1] recently used the OVERFLOW[2,3] code to simulate hover flight conditions for the Tilt Rotor Aeroacoustics Model (TRAM) isolated rotor over a range of collective angles. These time-accurate Reynolds-averaged Navier-Stokes (RANS) simulations were carried out in an inertial overset grid system. Body-fitted curvilinear grids attached to the rotor blades rotated through a fixed Cartesian grid system. The latter was used to resolve the vortex wake and extend the computational domain to the far field. Baseline computations were carried out on a wake grid with uniform grid spacing, Δ=10% c_{tip}. This is the approximate size of the physical vortex core diameter. The wake region was further resolved using a new dynamic Adaptive Mesh Refinement (AMR) procedure. Refined Cartesian grids were added or removed in the vortex-wake region based on a vorticity sensor function. Two levels of refinement were used (each level differs by a factor of two), so that the wake region was resolved with Cartesian grids whose grid spacing was Δ=10% c_{tip}, 5% c_{tip}, and 2.5% c_{tip}, see Fig. 1.

For the first time, the TRAM Figure of Merit (FM) was predicted within experimental error for a wide range of collective angles. This study had three important findings. First, fine surface-body grid resolution and the use of 5th-order spatial differences were more important to accurately predicting FM at a high-thrust condition (θ=14°) than resolving the wake vortices. Second, the FM was accurately predicted over a collective range of $6° \leq \theta \leq 16°$ using the Spalart-Allmaras (SA) turbulence model[4] together with the Detached Eddy Simulation[5-6] (DES) length scale. This was accomplished on the baseline grid system (uniformly spaced wake grids) without the expensive use of AMR.

The difference in predicted FM between the SA-RANS and SA-DES models is shown in Fig. 2. Note that the SA-DES turbulence model had excellent agreement with the experimental data over the entire range of collectives, but the SA-RANS model only agreed well at the high-thrust collectives. This marked difference between turbulence models occurs when there is Blade Vortex Interaction (BVI) between the tip vortices and the rotor blades. The DES length scale produces a much smaller Turbulent Eddy Viscosity (TEV). As long as there is no BVI, the RANS FM results are very good. However with BVI, the large TEV in the rotor wake can infiltrate the rotor blade boundary layer, increasing C_Q and greatly reducing the FM. Although DES was developed to resolve the largest eddies in a separated turbulent flow, DES was not used in this manner for the TRAM simulations. Rather, the more realistic DES turbulent length scale was used in the rotor wake to reduce the TEV and improve the prediction of FM.

A third finding[1] showed the new DES/AMR procedure produced a vortex wake rich in turbulent physics, see Figs. 1,3. The tip vortices were much stronger and had smaller core diameters than the baseline result. Moreover, vortical "worms" were found to encircle the tip vortices through a process of entrainment of the wake shear layers into the tip vortices and vortex stretching. The worms are less prevalent in the upper wake and quite dense in the lower wake due to the entrainment process. These simulations were for a rigid TRAM blade system.

Ahmad and Chaderjian[7] recently reported a significant improvement in the prediction of the normal force and pitching moments for the UH-60 rotor in forward flight. This was accomplished by loosely coupling the OVERFLOW code with the CAMRAD II helicopter comprehensive code.[8] CAMRAD II provided blade deformations and trim conditions, while OVERFLOW provided CFD loads from the RANS equations. The improvement of the predicted loads was attributed to improved surface-grid resolution and the use of 5th-order spatial differences in OVERFLOW.

The goal of this paper is to demonstrate OVERFLOW's new high-order spatial differencing, AMR process, and the use of the SA-DES turbulence model on the flexible UH-60 rotor in forward flight and hover. Moreover, attention will be given to the time accuracy of the numerical method, convergence of the loose-coupling process with AMR, and details of the UH-60 rotor wake in hover and forward flight.

The numerical approach is described in the next section, including a brief description of the CAMRAD II helicopter comprehensive code, fluid/structure loose coupling procedure, UH-60 geometry and overset grid system, flow-solver algorithm, dynamic AMR algorithm, and turbulence model. This is followed by a discussion of the numerical results and concluding remarks.

Numerical Approach

A numerical approach that is used to simulate the flow field for a flexible UH-60 rotor using the time-dependent Navier-Stokes equations is now described.

Comprehensive Code: CSD and Rotor Trim

The helicopter comprehensive code CAMRAD II[8] provides Computational Structural Dynamics (CSD) and rotor trim for a coupled CFD/CSD simulation. This code is widely used in the helicopter industry. It models the flexible rotor blade structure using nonlinear finite elements. CAMRAD II has its own simplified aerodynamic lifting-line model, a 2D airfoil table lookup for additional viscous realism, and tip-vortex wake models. Although this code has been widely used, its prediction capability is limited due to the low fidelity aerodynamic model. However, it has been used with high-fidelity CFD models in a loosely coupled manner. The details of this comprehensive code are

described by Johnson,[8] and the coupling strategy is described briefly below and in more detail by Potsdam et al.[9]

Fluid/Structure Interaction: Loose Coupling

For static flight conditions, a loose coupling procedure between CFD and CSD is employed. This coupling is done in a periodic manner, as specified by the user. The coupling period is some fraction of the number of rotor blades. In the case of the four-bladed UH-60 rotor, coupling periods of ¼, ½, and 1 revolution are typical. The lower coupling periods often provide faster loose-coupling convergence, provided the process is stable. More difficult cases, e.g., dynamic stall, may require larger coupling periods. A coupling period of ¼ revolution is used in this paper.

The coupling procedure is valid as long as the rotor loads are periodic. This does not preclude some aperiodicity in the vortex wake, which is often the case in a high-resolution turbulent flow simulation. If the rotor loads are not periodic, e.g., a maneuvering vehicle, then the procedure is not time accurate. In this case, a tight-coupling procedure is required.

At each coupling step, CFD rotor loads are provided to CAMRAD II and, in turn, it uses these CFD loads to make a correction to its own simplified aerodynamic model. CAMRAD II then goes through a CSD analysis and re-trims the rotor blade motions. CAMRAD II then provides a new rotor-blade deflection file to the CFD code. When this loosely coupled process is fully converged, the CFD airloads have fully replaced the CAMRAD II airloads.

Figure 4 shows a flow chart of the loose coupling iterative procedure. The detailed logistics for running the coupled CAMRAD II and OVERFLOW process is accomplished using a C-shell script. This script helps automate the run process, which uses many CAMRAD II tools and coupling steps. The reader is again referred to Refs. 8-9 for additional details.

Rotor Geometry/CFD Grid

The OVERFLOW 2.2 CFD code has been used for the UH-60 flow simulations presented in this paper. This code utilizes structured overset grids for this four-blade/simple-hub geometry. Figure 5 shows body and volume grids for the UH-60 rotor blades, and the locations of flight-test data. Near-body (NB) grids refer to the curvilinear grids attached to the rotor blades and hub. Off-body (OB) grids refer to all Cartesian grids. The O-grids on the rotor blades have 253x255x63 grid points in the chord, radial, and body-normal directions. There are ten grid cells across the blunt trailing edge. O-type cap grids are also used to resolve the inboard and outboard rotor-blade tips. All of the NB grids extend about one tip chord in the body normal direction, and have a total of 23 million grid points. A uniform Level-1 Cartesian grid is typically used to resolve the rotor-wake region with a spacing of $\Delta = 10\%\ c_{tip}$. Coarser "brick" grids are used to extend the computational domain to the far field. Each brick grid has a grid spacing that is twice as coarse as the previous one. Surface grid resolution follows the practice and recommendations of Ref. 1. The viscous wall spacing typically has a range of $0.5 \le y^+ \le 1.0$ on the blade surfaces.

Flow-Solver Algorithm

OVERFLOW is a finite-difference, overset grid, Navier-Stokes CFD code. Up to 6th-order spatial accuracy for inviscid fluxes and 2nd-order time accuracy are available.[10] OVERFLOW has two modes of operation, stationary grids and dynamic grid motions. In the case of grid movement, both rigid-body motions and deforming grids are permitted. Inter-grid overset communication can be established external to OVERFLOW using the PEGASUS code.[11] This is only done for non-moving grid cases. For the present dynamically moving grid simulations, inter-grid communication is established using X-Rays[3] and the very efficient Domain Connectivity Function[3] within OVERFLOW. OVERFLOW has several turbulence models available. For the present study, the one-equation Spalart-Allmaras model[4] is used. OVERFLOW has many flow-solver options described in Refs. 2-3. The effect of subiteration convergence on temporal accuracy is quantified in the Results section.

A 2nd-order accurate dual time-stepping algorithm is used to solve the RANS equations, and is based on the dual time-stepping methods described in Refs. 12-13. The dual time-stepping algorithm is now described, and subiteration accuracy is discussed in the results section.

The Navier-Stokes equations can be written in strong conservation-law form as

$$\frac{\partial Q}{\partial t} + \frac{\partial (F - F_v)}{\partial x} + \frac{\partial (G - G_v)}{\partial y} + \frac{\partial (H - H_v)}{\partial z} = 0 \qquad (1)$$

where $Q = [\rho \quad \rho u \quad \rho v \quad \rho w \quad e]^{\mathrm{T}}$ is the vector of conserved variables; F, G, and H are the inviscid flux vectors; and F_v, G_v, and H_v are the viscous flux vectors.

An artificial time term is introduced to the governing equations in order to provide a relaxation (subiteration) procedure between physical time steps.

$$\frac{\partial Q}{\partial \tau} + \frac{\partial Q}{\partial t} + \frac{\partial (F - F_v)}{\partial x} + \frac{\partial (G - G_v)}{\partial y} + \frac{\partial (H - H_v)}{\partial z} = 0 \qquad (2)$$

where t corresponds to physical time and τ corresponds to artificial (pseudo) time.

First-order accurate Euler implicit differencing is used for the artificial time discretization, while a second-order accurate three-point backward difference is used for the physical time discretization. An implicit approximate factorization form of Eq. (2) in generalized coordinates is given by

$$\left[I + h\partial_\xi \hat{A}^k\right]\left[I + h\partial_\eta \hat{B}^k\right]\left[I + h\partial_\zeta \hat{C}^k\right]\Delta\hat{Q}^k = -hR^{k,n} \qquad (3)$$

where

$$R^{k,n} = \frac{3\hat{Q}^k - 4\hat{Q}^n + \hat{Q}^{n-1}}{2\Delta t} + \left(\hat{F} - \hat{F}_v\right)_\xi^k + \left(\hat{G} - \hat{G}_v\right)_\eta^k + \left(\hat{H} - \hat{H}_v\right)_\zeta^k$$

and

$$h = \frac{2\Delta t \Delta\tau}{2\Delta t + 3\Delta\tau}$$

In these equations, $\hat{Q} = Q/J$, where J is the transformation Jacobian, and A, B, and C are the inviscid flux Jacobians. The variable k is the subiteration index, while the variable n is the time-step index. Finally, $\Delta\hat{Q}^k = \Delta\hat{Q}^{k+1} - \hat{Q}^k$. Subiteration convergence implies that $\hat{Q}^k \to \hat{Q}^{n+1}$, which is second order accurate in time.

A diagonalized implicit algorithm[14] is used to solve this equation, and central differences are used to discretize the spatial derivatives. Upwind difference options are available in OVERFLOW, but were not used in this study.

The central difference spatial accuracy consists of evaluating the convective terms with 6th-order central differences and 5th-order artificial dissipation. This results in a 5th-order accurate discretization on the uniform Cartesian OB grids. However, all viscous terms are evaluated with 2nd-order accurate central differences. The grid metrics on the curvilinear NB grids are also 2nd-order accurate in space. This discretization is referred to as 5th-order spatial differencing throughout this paper. Although the algorithm is still formally 2nd-order accurate in space, this differencing scheme has lower diffusion and dispersion errors, and an improved flow field resolution than a 3rd-order approach. Table 1 summarizes the convective central difference operators. Further details are described by Pulliam.[10]

Dynamic AMR Algorithm

A dynamic AMR capability has been included in OVERFLOW, where Cartesian grids are automatically added in the rotor wake region to improve the resolution of the wake vortices. This is done internally to the OVERFLOW code in a time-accurate manner with moving rotor blades. This procedure is now briefly described.

The concept of Level 1 grids and brick grids have already been introduced. The brick grids are successively coarsened by factors of two from the original Level 1 grid, to extend the computational domain to the far field. For example, if Δ_1 is a user-specified spacing for the Level 1 grids (baseline Cartesian wake grids), then the coarser brick grids have grid spacing of $\Delta_2=2\Delta_1$, $\Delta_3=4\Delta_1$, $\Delta_4=8\Delta_1$, and so on. In a similar manner, if a Level 1 region is tagged for grid refinement, e.g., to better resolve a vortex core, then the grid spacing has the following form: $\Delta_{-1}=\frac{1}{2}\Delta_1$, $\Delta_{-2}=\frac{1}{4}\Delta_1$, $\Delta_{-3}=\frac{1}{8}\Delta_1$, and so on. A sensor function based on the vorticity magnitude is used to identify where to refine the OB Cartesian grids.

The dynamic AMR process is described in more detail by Buning and Pulliam,[15] and Chaderjian and Buning.[1] Figure 1 is an example of a two-level AMR OB refinement for the TRAM rotor in hover.

Turbulence Model

The OVERFLOW code has a choice of algebraic, one-equation and two-equation turbulence models[2-3] that close the system of RANS equations. The UH-60 rotor simulations presented in this study use the one-equation Spalart-Allmaras[4] (SA) turbulence model. The details of the SA turbulence model play an important role in controlling the TEV levels in the flow, the numerical diffusion of the rotor tip vortices, and the accurate prediction of FM.[1] Some of the key features of this model are now discussed.

The SA model uses the Boussinesq approximation to relate the Reynolds stresses to a kinematic turbulent eddy viscosity and the mean strain-rate tensor. The TEV is given by the expression

$$\nu_t = \tilde{\nu} f_{v1}$$

The SA turbulent transport equation for the turbulence variable $\tilde{\nu}$, is given by

$$\frac{D\tilde{\nu}}{Dt} = P(\tilde{\nu}) - D(\tilde{\nu}) + \mathcal{D}(\tilde{\nu}) \tag{4}$$

where D/Dt is the material time derivative. The right hand side consists of production, dissipation and diffusion source terms. The production is given by

$$P(\tilde{\nu}) = C_{b1}\tilde{\nu}\left(\Omega + \frac{\tilde{\nu}}{\kappa^2 d^2} f_{v2}\right) \tag{5}$$

the dissipation by

$$D(\tilde{\nu}) = C_{w1} f_w \left(\frac{\tilde{\nu}}{d}\right)^2 \tag{6}$$

and the diffusion by

$$\mathcal{D}(\tilde{\nu}) = \frac{1}{\sigma}\left[\nabla\bullet\left((\nu + \tilde{\nu})\nabla\tilde{\nu}\right) + C_{b2}(\nabla\tilde{\nu})^2\right] \tag{7}$$

The constants C_{b1}, C_{b2}, C_{w1}, κ, σ, and functions f_{v1}, f_{v2}, f_w, are described by Spalart and Allmaras.[4] The damping function, f_{v1}, reduces ν_t near a solid wall. The turbulent length scale, d, is defined as the distance to the nearest wall.

The SA model was originally developed for boundary-layer flows, where d is a reasonable length-scale estimate of the largest energy-bearing turbulent eddies. In vortex dominated flows, such as in a rotor wake, the distance from the vortex core to the nearest wall can be very large, even several rotor radii, and produce very large TEV. This has the effect of greatly diffusing the wake vortices and reduces the predicted FM.

Shur et al.[16] introduced a correction for rotating and curved flows, which is referred to as the SARC correction. The SARC correction not only improves the boundary-layer profiles for highly curved flows, but also helps reduce the TEV in the vortex wake cores. The SARC correction is used in the present reported results. It is also noted that in the rotor wake, where the length scale $d \to$large, the dissipation term $D \to 0$. So there is no significant TEV dissipation in the rotor wake. TEV can therefore be locally produced and diffused, but not dissipated. The lack of TEV

dissipation in the wake can be a problem, especially for hover simulations, even with the SARC correction.

An additional degree of realism can be realized by the use of Large Eddy Simulation (LES). LES is a computation where the largest turbulent eddies are resolved with small grid spacing, Δ, and the subgrid-scale (SGS) eddies are modeled. Smagorinsky[17] first postulated a SGS model for the Reynold's stresses based on the following expressions

$$\tau_{ij} = 2\nu_t S_{ij}, \;\; S_{ij} = \frac{1}{2}\left(\frac{\partial \bar{u}_i}{\partial x_j} + \frac{\partial \bar{u}_j}{\partial x_i}\right) \tag{8}$$

where S_{ij} is the resolved mean strain rate, ν_t is the Smagorinsky eddy viscosity given by

$$\nu_t = \left(C_s \Delta\right)^2 \sqrt{S_{ij} S_{ij}} \tag{9}$$

and C_s is the Smagorinsky coefficient. In this expression, $\Delta=(\Delta x\ \Delta y\ \Delta z)^{1/3}$, i.e., the geometric mean of the grid cell spacing. LES is beyond the scope of all but the most fundamental of turbulent flow computations. However, Spalart et al.[5] suggested Detached Eddy Simulation (DES) as a more practical alternative.

DES can be viewed as a blending of a RANS turbulence model in boundary layers, and coarse-mesh LES in regions of flow separation, or where the largest eddies are to be grid resolved. This is accomplished in the SA model by replacing the distance to the nearest surface (d) by

$$\bar{d} = \min\left(d, C_{DES}\Delta\right) \tag{10}$$

where $\Delta=\max(\Delta x, \Delta y, \Delta z)$, and $C_{DES}=0.65$. So the SA RANS model becomes the SGS model. Moreover it is easy to see that when production balances dissipation (Eqs. 5-6), e.g., when Δ is small, then ν_t simplifies to a Smagorinsky-type model. So the SA-DES model behaves like an LES-type model when the grid spacing is sufficiently small.

The primary use of Eq. 10 in the present rotor simulations is to obtain a more realistic turbulent length scale in the rotor wake. This insures the magnitude of TEV is controlled so that in BVI cases, an excessively large TEV does not infiltrate the blade boundary layers and artificially reduce the FM through an increased C_Q. However, with the introduction of finer AMR grids, the largest eddies in the turbulent wake are beginning to be resolved.

At this point a few cautionary comments on the application of DES are in order. First, it is a common mistake to claim a DES simulation by simply turning on Eq. 10. Note that "RANS" grid spacing in the wall-parallel direction will not cause Eq. 10 to switch to the DES length scale. In other words, one is still left with a pure RANS result.

A second danger occurs when using excessive grid refinement near a solid wall, or a boundary layer gradually approaching separation. The intended use of DES is to be in RANS mode throughout the boundary layer, where the turbulent scales can be very small, and LES mode outside the boundary layer, where the turbulent scales are larger, e.g., separated flow. This occurs when the wall-parallel spacing $\Delta\| > \delta$. If the wall-parallel grid spacing is much smaller than the boundary layer thickness ($\Delta\| \approx d/20$ is a plausible starting point), then LES resolution applies within the upper portion of the boundary layer, and very close to the wall the RANS model acts as an appropriate sub-grid model. In-between these two examples, the grid spacing is ambiguous, being neither RANS nor LES. In these cases the turbulent shear stresses are too small within the boundary layer due to inadequate grid support for the full range of turbulent length scales. This modeled stress depletion (MSD) can trigger premature separation, and give non-physical results.

This situation can be avoided by making sure the grid spacing parallel to the wall is larger than the attached boundary layer thickness. However, Spalart et al.[6] introduce a correction called Delayed Detached Eddy Simulation (DDES). This algebraic formula prevents the inadvertent use of LES mode within a boundary layer, ensuring that the RANS model is active throughout that region. Details of the DDES modification are given in Ref. 6.

DDES is used throughout this paper, even though the wall-parallel grid spacing used is not so small as to require DDES. Nonetheless, DDES has been used as a precaution.

Numerical Results

The goal of this research is to demonstrate OVERFLOW's new high-order spatial differencing, the AMR process, and the use of the SA-DES turbulence model on the UH-60 flexible-blade rotor in forward flight and hover. Loosely coupling the OVERFLOW and CAMRAD II codes is needed to account for the UH-60's flexible rotor blades. However, this research emphasizes high-order spatial differences and high resolution OB wake grids as part of a multidisciplinary process. A forward flight and hover condition will be presented in this paper.

NASA and the US Army, as a part of the UH-60 Airloads program, maintain an extensive flight-test database[18] for level flight and transient maneuvers. The database provides aerodynamic pressures, structural loads, control positions, and rotor forces and moments. This database is extensively used for the validation of both aerodynamic and structural models. The test matrix provides a range of flight conditions. Flight counter C8534 is a high-speed level-flight case that is explored in this paper. The advance ratio is $\mu = 0.37$, the freestream Mach number is $M_\infty=0.236$, and the tip Mach number is $M_{tip}=0.64$. Reference 18 mentions that many investigations have been performed on this flight-test counter to understand unsolved analysis problems for the advancing blade azimuthal phase lag and under-prediction of blade pitching moments. A fuselage was not included in these simulations.

A hover flight condition is also explored. Wind tunnel measurements were obtained at the United Technologies Research Center (UTRC) wind tunnel.[19] This data is generally accepted as being the most reliable and comprehensive hover data, and includes wake trajectory, blade loading, blade deformations, and performance measurements. Wind tunnel measurements were also obtained at the Duits-Nederlandse Windtunnel (DNW).[20] The CFD simulations correspond to the UTRC wind tunnel test, where $M_{tip}=0.628$, $C_T/\sigma=0.102$, $\sigma=0.0825$, and FM=0.734. The blade deformations were also measured and used in the CFD simulations in an uncoupled manner.

Forward Flight (C8534)

Flow simulations are carried out using a 2nd-order accurate dual-time sub-iteration method described in the Flow-Solver Algorithm section. It is therefore important to establish the time step and number of sub-iterations to insure temporal sub-iteration convergence and proper resolution of the relevant frequencies. The approach taken here is to examine how these two parameters affect the normal force and pitching moment coefficients over one period (¼ revolution for this four-bladed rotor). An OVERFLOW solution was first obtained using the grid shown in Fig. 5 with an uncoupled CAMRAD II motion file (from CAMRAD's aerodynamics model). This is the starting point for this time-accuracy study.

A baseline time step, Δt=¼ deg rotor rotation, is used based on previous experience.[1,7] Figure 6 shows how the number of dual-time sub-iterations (N_i) affects the convergence of the dual-time algorithm, the total normal force (C_N), and total pitching moment (C_M) coefficients over ¼ rotor revolution. The dual-time sub-iteration convergence drops with increasing N_i, with decreasing effectiveness at the larger values. The percent RMS difference between the C_N and C_M waveforms and their waveforms at 100 sub-iterations does not show a monotone decrease with the number of sub-iterations until N_i=35. This is the beginning of the asymptotic region, and corresponds to a dual-time sub-iteration drop of about 2.5 orders in magnitude, somewhat lower than the 2-order drop rule of thumb. Favorable CFD comparisons that are not in the asymptotic range may simply be fortuitous and can potentially get worse with more convergence. The percent RMS difference in C_N and C_M is less than 1% when N_i=40. Figure 7 shows how the number of sub-iterations affects the C_N waveforms.

Figure 8 shows how the C_N and C_M waveforms converge with time step when N_i=40. Percent RMS differences are formed between the C_N and C_M waveforms and their respective waveforms at Δt=1/32 deg. This reference time step is very small and considered more than adequate for the present flow simulations. Both the C_N and C_M waveforms are in the asymptotic range (monotone convergence) when $\Delta t \leq$¼ deg. Based on the results shown in Figs. 6-8, flow simulations for the rest of this paper use Δt=¼ deg, and N_i=40.

Now that the dual-time stepping parameters have been established for 2nd-order time accuracy, loosely coupled Overflow/CAMRAD II simulations are carried out for two different OB wake-grid resolutions. Adaptive mesh refinement is used in both cases to insure the rotor wake is covered by the desired grid resolution. The baseline case (AMR0) is shown in Fig. 9, where the wake is resolved by an OB grid spacing Δ=10% c_{tip}. Note that the rotor is embedded within a tight "box grid", and the AMR process finds the vortical wake and automatically adds additional grids with the same resolution. This overset grid system uses 960 grids with a total of 61 million grid points. This is more computationally efficient than selecting a large "box grid" to cover the entire wake region. Moreover, this eliminates the need to estimate the wake position prior to computing the flow. The second AMR wake resolution is four times finer, adding two more levels of refined Cartesian grids to the wake. So the wake is now resolved by Cartesian grids with grid spacings Δ=10%, 5%, and 2.5% c_{tip}. This grid system, which has about 18,500 grids and 754 million grid points, is shown in Fig. 10 and designated as AMR2 (for two levels of refinement).

The loosely coupled AMR0 case began from impulsive-start conditions and ran for 4.5 rotor revolutions. This allowed ample time for the wake to develop and the rotor loads to be established. The AMR2 case started from the AMR0 result at 3 revs and run an additional 5 revs. OVERFLOW and CAMRAD II exchanged data in a loose coupling manner every ¼ revolution. Figures 11-13 show the blade pitch, flap, and lag angles, including the 1st harmonics, for each loose coupling step for the AMR2 grid system. These plots also include the first 3 revs (11 coupling steps) of the AMR0 case, which served as the starting point for the fine-grid AMR result. The blade control angles are converged in the AMR0 result by the 3rd revolution (11 coupling steps). Continuing with the AMR2 result did not alter the blade control angles in any significant manner.

Figure 14 shows the RMS difference between the C_N and C_M waveforms between successive coupling steps. The normal force coefficient shows a 1.5 order drop while the pitching moment coefficient shows almost a 2.0 order drop. Both the AMR0 and AMR2 grids systems are equally converged. It is not possible to converge these flows further as the force/moment differences are quite small, and change slightly with time due fluid dynamic nonlinearities. Figure 15 shows that the converged sectional normal force and pitching moment coefficients at r/R=0.865 are virtually indistinguishable between coupling steps for both grid systems.

Figure 16 shows the rotor wake system for the baseline AMR0 grid system. The tip vortices and some of the blade trailing-edge shear layers are rendered with iso-surfaces of the Q-criterion. The vortex core diameters are much larger, and the core vorticity is greatly diffused, compared to the physical vortex cores. This is because the grid spacing, Δ=10%c_{tip}, is about the size of the physical vortex cores. The simplified hub sheds a stream of eddies that engulf the inboard portion of the rotor blade at ψ=0°, and convect downwind.

Figure 17 shows the rotor wake system for the AMR2 grid system, where the finest OB Cartesian grids are 4x finer than the AMR0 grid system. Note that the vortex cores are much smaller in diameter than the baseline system. Fine details of the blade trailing-edge shear layers are clearly seen, and the interaction of these wake shear layers with the vortex cores produces some vortical worms, similar to the TRAM rotor in hover.[1] The turbulent eddies shed from the rotor hub are smaller and have greater detail than the coarse-grid result.

A comparison between the computed sectional pitching moment and normal force coefficients with flight-test data at four radial blade stations is shown in Figs. 18-19. The computed values are in good overall agreement with the measurements. The mean normal force and pitching

moment coefficients evaluated over one rotor revolution agree with the flight-test values within 2.1% and 2.5%, respectively. The AMR0 and AMR2 M^2C_m and M^2C_n are virtually identical. This is not surprising since there is no significant BVI to affect the rotor loads. Higher grid resolution in the vortex wake may improve the rotor load prediction when there is significant BVI. High resolution wakes can also be important in studying interactional aerodynamics between the rotor vortices and other vehicle components, including the prediction of vehicle vibration and sound levels.

Hover

OVERFLOW is used to simulate the UH-60 rotor in hover, and the results are compared with UTRC[19] and DNW[20] wind-tunnel data. The CFD simulation corresponds to the UTRC wind-tunnel test, where M_{tip}=0.628, C_T/σ=0.102, σ=0.825, and FM=0.734. The UTRC measured blade deflections are used to model the flexible rotor blades. So there is no loose coupling between OVERFLOW and CAMRAD II for this case.

The wind-tunnel UH-60 rotor model, unlike the flight-test rotor, does not have an outboard trim tab. The near-body grids used in the previous forward-flight simulation have a trim tab, and will be used for the hover computations. Two different OB wake resolutions will be used: 1) AMR0, where Δ=10%c_{tip}; and 2) AMR1, where Δ=10% and 5%c_{tip}. Note that only one level of grid refinement is used here. The rotor wake will be resolved up to 2 rotor radii below the rotor disk. Using two levels of refinement would yield a grid system in excess of 1 billion grid points. One AMR0 result without a blade trim tab will be simulated and compared with the trim tab results to determine how the trim tab may affect the computed results and comparison with experiment.

Figure 20 shows the baseline AMR0 grid at the y=0 plane. There are about 1800 grids with a total of 78 million grid points. The Cartesian grids are capturing the tip vortices but do not capture the hub wake very well. This under-resolved center region falls below the vorticity magnitude sensor threshold. Figure 21 shows the AMR1 grid. The finer resolution captures both the tip vortices and the hub wake with about 7700 grids and 302 million grid points.

The AMR0 case starts from impulsive start and runs for 22 revolutions. Unlike forward flight, hover simulations have lower, self-induced flow, which takes longer to develop. The AMR1 case starts from the AMR0 result at 17 revs and runs an additional 5 revs for a total of 22 revs. Figure 22 shows the time evolution of the FM, its running mean (based on 1 rev period), and the standard deviation. At 22 revs, the FM running mean has settled to a value where the 3rd digit is stationary.

Figure 23 shows a plot of the UTRC and DNW FM measurements verses thrust coefficient. The UTRC data is considered by many to be more reliable than the DNW data, which was smoothed due to variability in the data. The DNW FM also tends to be high. The uncertainties in the measured FM are unknown. Three OVERFLOW FM solutions are also shown on the figure, corresponding to AMR0 without a trim tab, AMR0 with a trim tab, and AMR1 with a trim tab. All three are summarized in Table 2, along with the accepted UTRC value for FM. All three computed FM are within 0.001 of each other, and differ from the UTRC value by 2%. This is a good comparison with the measured data in light of the lack of knowledge of the measurement uncertainty.

Figure 24 compares the sectional thrust coefficient with the UTRC wind-tunnel data. Overall, all three solutions are in good agreement with the data and each other. The trim tab grids show a small oscillation in C_t at the trim tab edges. This is due to coarse radial grid spacing at the trim tab edges. It is also interesting to note that the C_t is slightly lower along the trim tab than the no-trim-tab result and wind tunnel data. These differences are small.

Figures 25-26 show vorticity magnitude contours on the y=0 plane for the AMR0 and AMR1 trim tab grid systems. The finer grid result looks more developed with much greater detail. Figures 27-28 show a cut-away view of the vortex wake system, where vortical flow is rendered using iso-surfaces of the Q-criterion. The difference in vortical resolution is dramatic, even though the AMR1 grid is only twice as fine as the AMR0 grid. The AMR0 and AMR1 results illustrate the unique application of DES to rotor wake simulation. In the case of the coarser wake grid resolution (AMR0, Fig. 27) the DES length scales serves to reduce the TEV down to more realistic values than the pure RANS length scale. This application improves the FM prediction in BVI cases from the pure RANS approach, and does not cause additional degradation of the tip vortices. It is clear from Fig. 27 that even the largest turbulent structures are under resolved. However, the application of DES on the finer wake grid (AMR1, Fig 28) illustrates how DES can be used to resolve the larger turbulent scales.

The UH-60 results in Fig. 28 exhibits a proliferation of vortical worms that is similar to DES simulations of the Tram Rotor,[1] see Fig. 3. These turbulent worms are caused by the blade tailing-edge shear layers moving downward at a greater rate than the tip vortex helix. When a shear layer passes by a vortex core, it is partially entrained into the vortex core. As the vortex tubes in the shear layers wrap around the vortex cores, they are stretched and increase in vorticity magnitude because of conservation of angular momentum. The size of these worms are similar to the TRAM worms, being slightly larger in diameter due to the coarser UH-60 wake grids. The TRAM wake grid was resolved to Δ=2.5% c_{tip}.

All CFD simulations were run on the NASA Pleiades Supercomputer system using Intel 2.93GHz Westmere nodes. Each node has 12 cores with 24 GB of memory. The computer runtimes for the forward flight and hover cases are summarized in Table 3.

Conclusions

The OVERFLOW Navier-Stokes code has been loosely coupled with the CAMRAD II comprehensive code to simulate the viscous flow for a flexible UH-60 rotor and simplified hub in forward flight. OVERFLOW also

simulated the UH-60 rotor in hover using a blade deflection file obtained from wind tunnel measurements. All simulations used 2nd-order dual-time accuracy, 5th-order central differencing, Cartesian Adaptive Mesh Refinement (AMR) in the rotor wake, and the Spalart-Allmaras Detached Eddy Simulation (DES) hybrid turbulence model. A number of key findings are summarized below.

- Time accuracy was established within the asymptotic range.
- The loose coupling process converged rapidly, even when using AMR
- AMR successfully found and resolved the rotor tip vortices and wake shear layers up to 4x finer than the baseline wake grid spacing.
- AMR can be used with a fixed wake grid spacing to more efficiently capture the rotor wake without apriori knowledge of the wake shape.
- The computed mean C_N and C_M for forward flight (C8534) agreed with experiment to 2.1% and 2.5%, respectively.
- Computed FM agreed with experiment to 2%. Computations with and without a trim tab had little affect on the FM and sectional thrust coefficient.
- Complex turbulent wakes and shear layers were captured, including the production of vortical worms through a process of wake shear-layer entrainment into the tip vortices and vortex stretching. This is similar to the TRAM results reported in Ref. 1.
- AMR in the rotor wake had little affect on the rotor loads for the weak BVI cases examined in this paper.

Acknowledgments

The authors would like to thank Mr. Timothy Sandstrom for generating truly state-of-the-art flow visualization. This work was funded by NASA's Subsonic Rotary Wing Project, and utilized the Pleiades supercomputer at NASA's Advanced Supercomputing (NAS) Division.

References

[1]Chaderjian, N. M., and Buning, P. G., "High Resolution Navier-Stokes Simulation of Rotor Wakes," Proceedings of the American Helicopter Society 67th Annual Forum, Virginia Beach, VA, May 3-5, 2011.

[2]Nichols, R., Tramel, R., and Buning, P., "Solver and Turbulence Model Upgrades to OVERFLOW 2 for Unsteady and High-Speed Flow Applications," AIAA-2006-2824, June 2006.

[3]Nichols, R., and Buning, P., "User's Manual for OVERFLOW 2.1," University of Alabama at Birmingham, Birmingham, AL, 2008.

[4]Spalart, P. R., and Allmaras, S. R., "A One-Equation Turbulence Model for Aerodynamic Flows," AIAA-92-0439, January 1992.

[5]Spalart, P., Jou, W-H., Strelets, M., and Allmaras, S. "Comments on the Feasibility of LES for Wings and on a Hybrid RANS/LES Approach," First AFOSR Conference on DNS/LES, August 1997, Greyden Press, Columbus, OH.

[6]Spalart, P. R., Deck, S., Sur, M. L., Squires, K. D., Strelets, M. and Travin, A., "A New Version of Detached-Eddy Simulation, Resistant to Ambiguous Grid Densities," *Theoretical and Computational Fluid Dynamics (2006)*, Vol. 20, No. 3, pp. 181-195.

[7]Ahmad, J. U., and Chaderjian, N. M., "High-Order Accurate CFD/CSD Simulation of the UH-60 rotor in Forward Flight," AIAA-2011-3185, June 2011.

[8]Johnson, W., "Rotorcraft Aerodynamic Models for a Comprehensive Analysis," American Helicopter Society 54th Annual Forum, Washington, D.C., May 1998.

[9]Potsdam, M., Yeo, H., and Johnson, W., "Rotor Airloads Prediction Using Loose Aerodynamic/Structural Coupling," *Journal of Aircraft*, Vol. 43, No. 3, May-June 2006, pp. 732-742.

[10]Pulliam, T. H., "High Order Accurate Finite-Difference Methods: as seen in OVERFLOW," AIAA-2011-3851, June 2011.

[11]Rogers, S. E., Suhs, N. E., and Dietz, W. E., "PEGASUS 5: An Automated Pre-Processor for Overset-Grid CFD," *AIAA Journal*, Vol. 41, No. 6, June 2003, pp. 1037-1045.

[12]Pulliam, T. H., "Time Accuracy and the Use of Implicit Methods," AIAA-93-3360, 1993.

[13]Venkateswaran, S., and Merkle, C. L., "Dual Time Stepping and Preconditioning for Unsteady Computations," AIAA-95-0078, 1995.

[14]Pulliam, T. H., and Chaussee, D. S., "A Diagonal Form of an Implicit Approximate-Factorization Algorithm," *Journal of Computational Physics*, Vol. 39, No. 2, 1981, pp. 347-363.

[15]Buning, P. G., and Pulliam, T. H., "Cartesian Off-Body Grid Adaption for Viscous Time-Accurate Flow Simulations," AIAA-2011-3693, June 2011.

[16]Shur, M. L., Strelets, M. K., Travin, A. K., and Spalart, P. R., "Turbulence Modeling in Rotating and Curved Channels: Assessing the Spalart-Shur Correction," AIAA *Journal,* Vol. 38, No. 5, May 2000, pp. 784-792.

[17]Smagorinsky, J., "General Circulation Experiments with the Primitive Equations. I. The Basic Experiment," *Monthly Weather Review*, Vol. 91, No. 3, 1963, pp. 99-164.

[18]Bousman, W. G., and Kufeld, R. M., "UH-60A Airloads Catalog," NASA TM 2005-212827, Aug. 2005.

[19]Lorber, P. F., Stauter, R. C., and Landgrebe, A. J., "A Comprehensive Hover Test of the Airloads and Airflow of an Extensively Instrumented Model Helicopter Rotor," Proceedings of the 45th Annual Forum of the American Helicopter Society, Boston, MA, May 1989.

[20]Lorber, P. F., "Aerodynamic Results of a Pressure-Instrumented Model Rotor Test at the DNW," Proceedings of the 46th Annual Forum of the American Helicopter Society, Washington D.C., May 1990.

Cartesian Wake Grid Accuracy	Difference Stencil	Artificial Dissipation
$O(\Delta X^2)$	$\delta_X^{(2)}$	$\sim(\Delta X^3)\delta_{X^4}$
$O(\Delta X^3)$	$\delta_X^{(4)}$	$\sim(\Delta X^3)\delta_{X^4}$
$O(\Delta X^4)$	$\delta_X^{(4)}$	$\sim(\Delta X^5)\delta_{X^6}$
$O(\Delta X^5)$	$\delta_X^{(6)}$	$\sim(\Delta X^5)\delta_{X^6}$
$O(\Delta X^6)$	$\delta_X^{(6)}$	$\sim(\Delta X^7)\delta_{X^8}$

Table 1 Convective central difference operators.

Overflow Grid Resolution	FM
AMR0 with trim tab	0.719
AMR1 with trim tab	0.718
AMR0 without trim tab	0.720
UTRC Wind Tunnel	0.734

Table 2 Computed and measured FM.

Case	Grid Points (millions)	No. Cores	hr/rev
C8534 AMR0	61	1536	5.4
C8534 AMR2	754	3072	23.8
Hover AMR0	78	1536	5.8
Hover AMR1	302	4608	10.1

Table 3 Computer run time for forward flight and hover cases using 2.93 GHz Intel Westmere nodes.

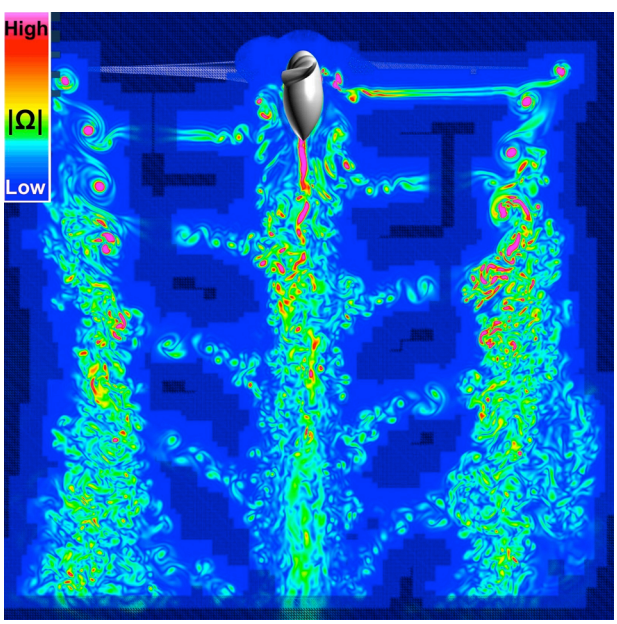

Figure 1. Vorticity magnitude on the y=0 cutting plane. AMR wake grid spacing: ΔS=10% c_{tip}, 5% c_{tip}, and 2.5% c_{tip}. TRAM rotor, M_{tip}=0.625, θ=14°, Re=2.1 million, Ref. 1.

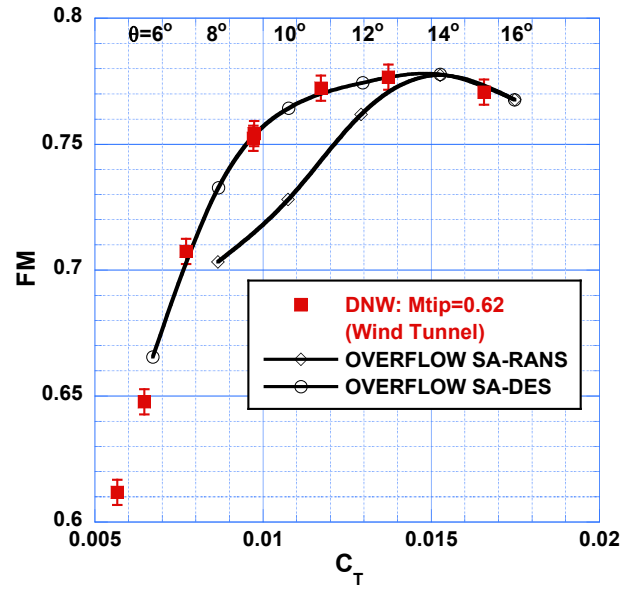

Figure 2. Figure of merit variation with C_T for the TRAM rotor in hover. Baseline wake grid spacing: ΔS=10% c_{tip}. M_{tip}=0.625, Re=2.1 million, Ref. 1.

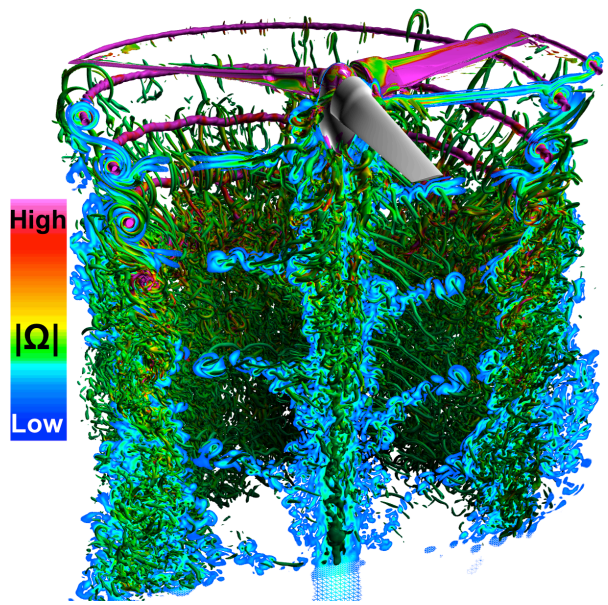

Figure 3. Cut-away view of vortex wake. AMR wake grid spacing: ΔS=10% c_{tip}, 5% c_{tip}, and 2.5% c_{tip}. TRAM rotor, M_{tip}=0.625, θ=14°, Re=2.1 million, Ref. 1.

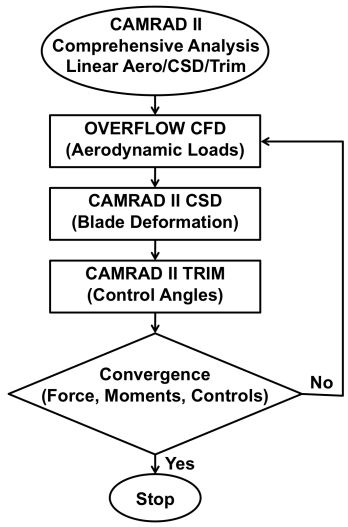

Figure 4. Loose coupling procedure with OVERFLOW and CAMRAD II.

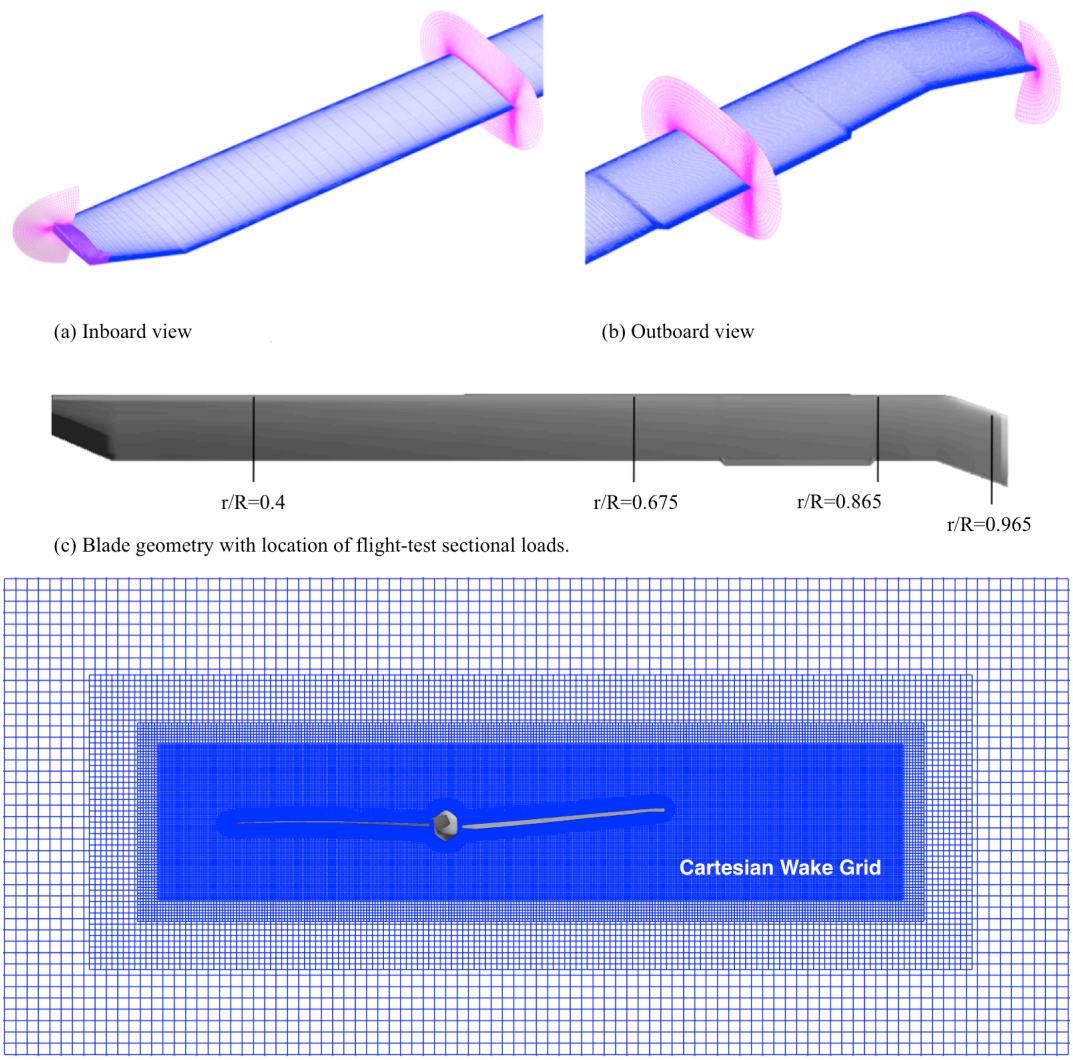

(a) Inboard view

(b) Outboard view

(c) Blade geometry with location of flight-test sectional loads.

(d) Body grids embedded into Cartesian wake grid.

Figure 5. UH-60 rotor/hub grid system.

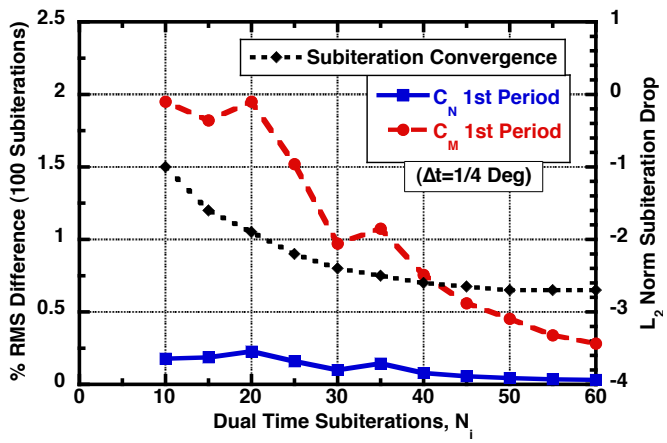

Figure 6. Convergence history of the dual-time algorithm, C_N and C_M with dual-time sub-iterations.

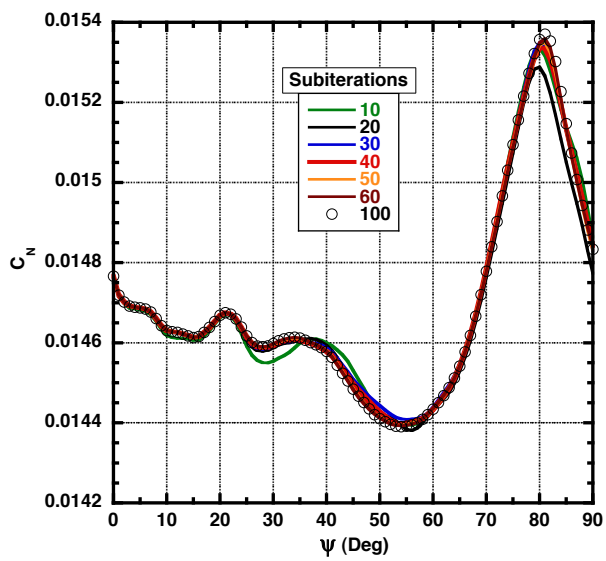

Figure 7. Normal force coefficient waveforms.

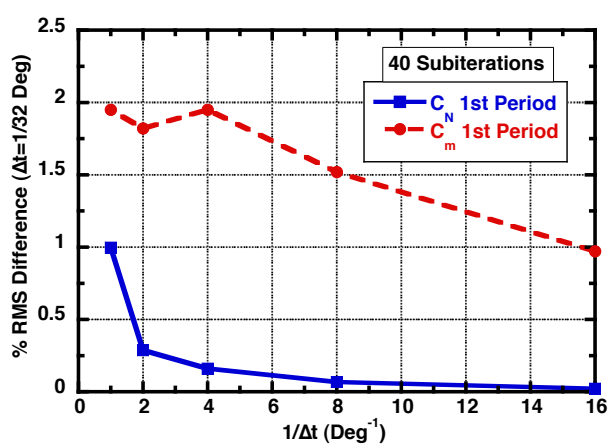

Figure 8. Convergence history of the C_N and C_M with time step.

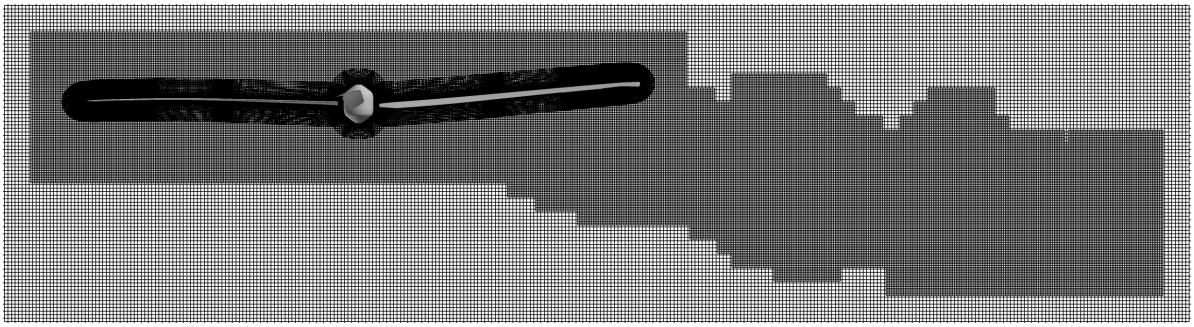

Figure 9. Baseline AMR0 grid system, Δ=10% c_{tip}, 960 grids, 61 million grid points, C8534.

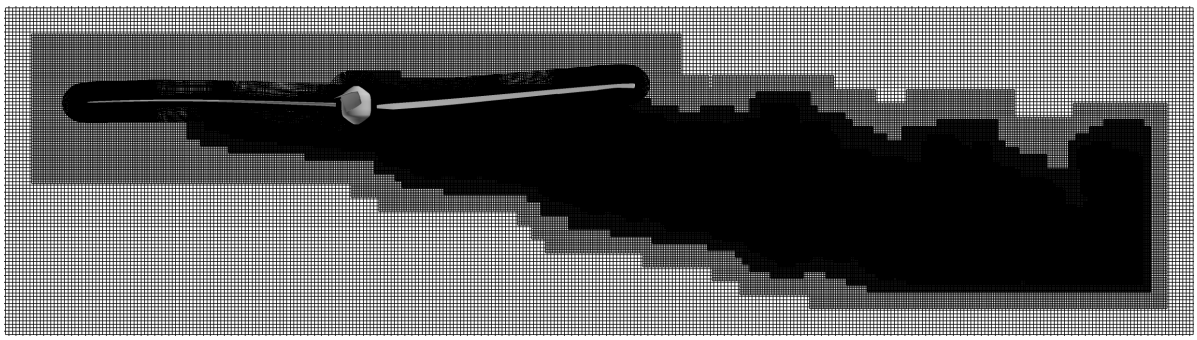

Figure 10. AMR2 grid system, Δ=10%, 5%, and 2.5% c_{tip}, 18,500 grids, 754 million grid points, C8534.

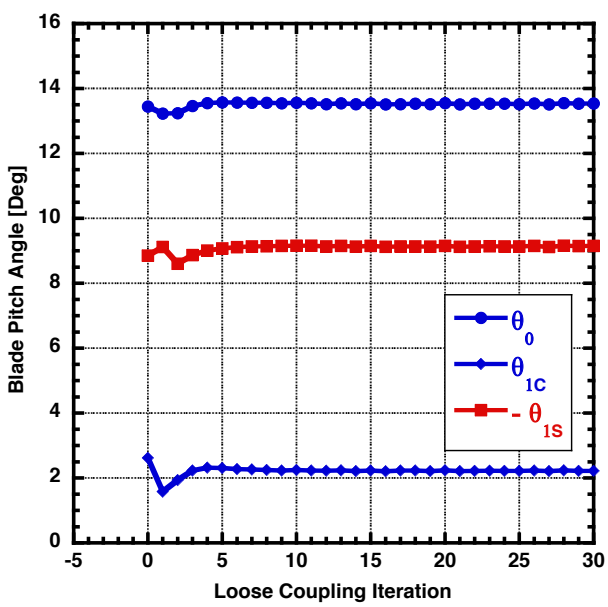

Figure 11. Loose coupling convergence history of the AMR2 blade pitch angles.

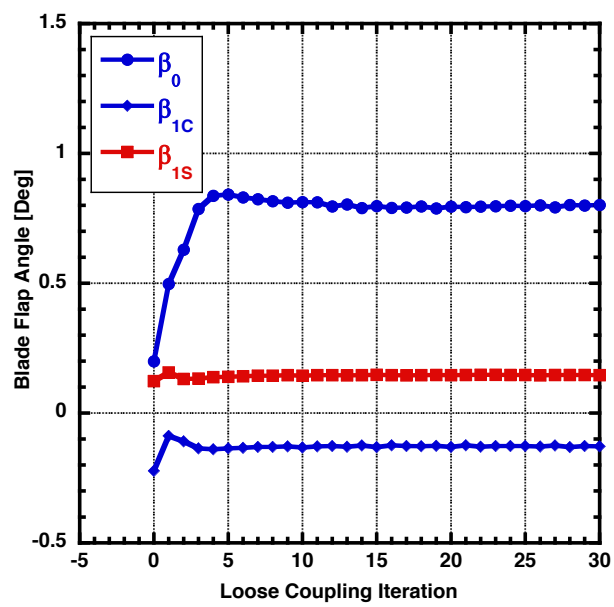

Figure 12. Loose coupling convergence history of the AMR2 blade flap angles.

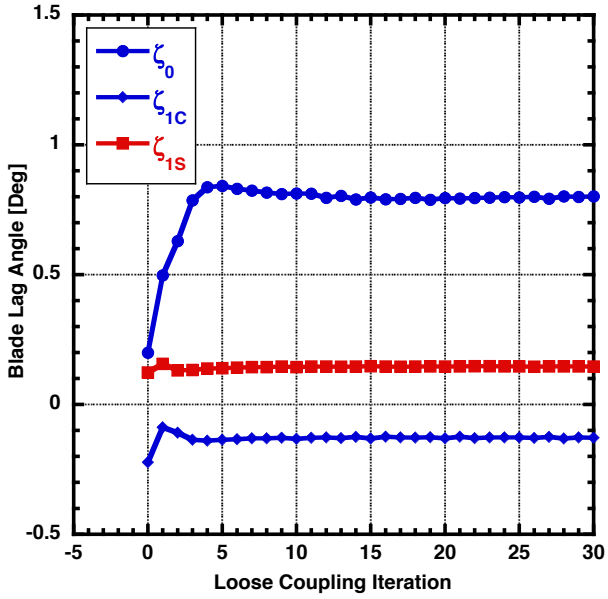

Figure 13. Loose coupling convergence history of the AMR2 blade lag angles.

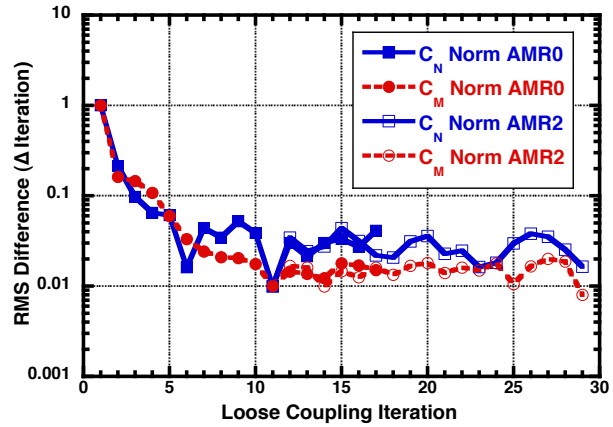

Figure 14. Loose coupling convergence history of the total normal force and pitching moment coefficients.

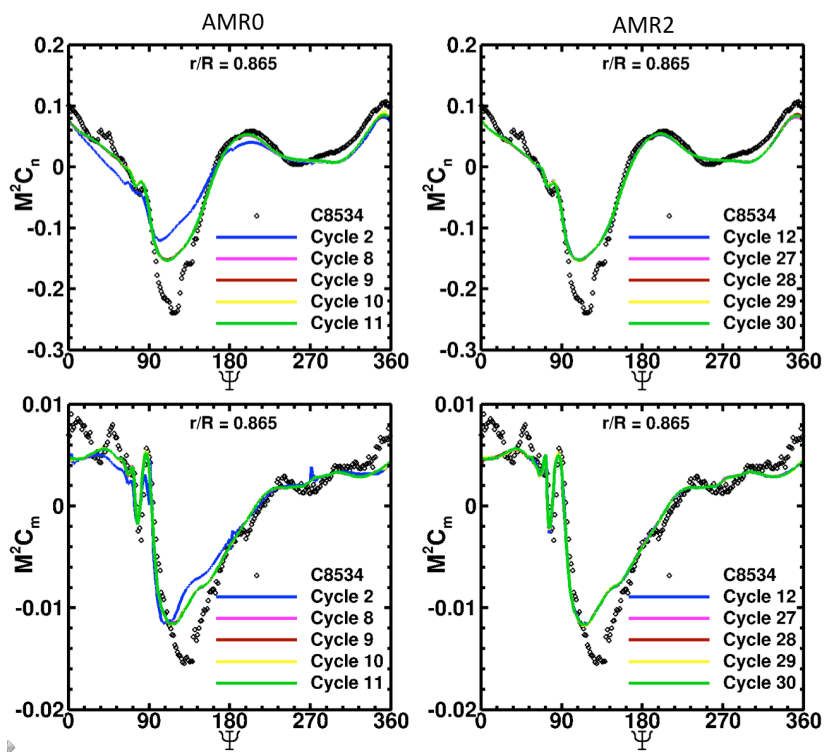

Figure 15. Loose coupling convergence of the sectional normal force and pitching moment coefficients at r/R=0.865.

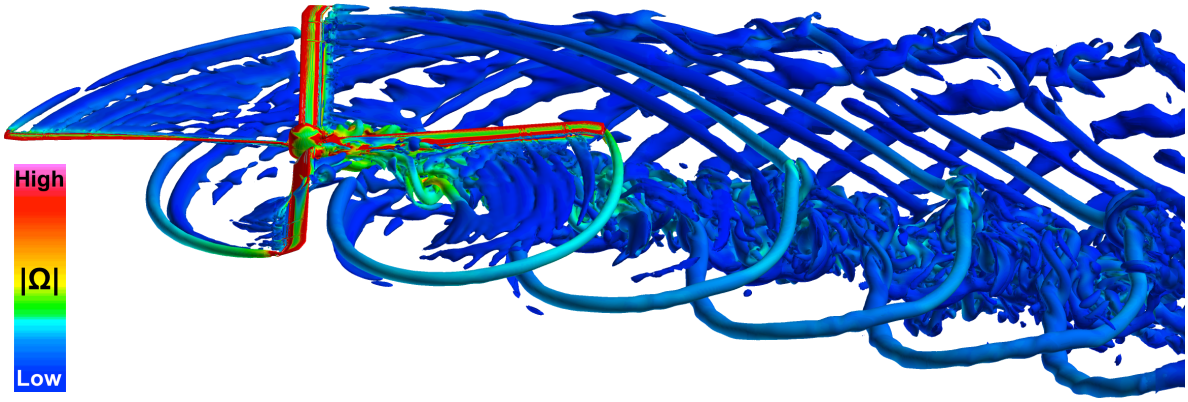

Figure 16. Baseline AMR0 vortex wake. Vortices rendered with the Q-criterion, C8534.

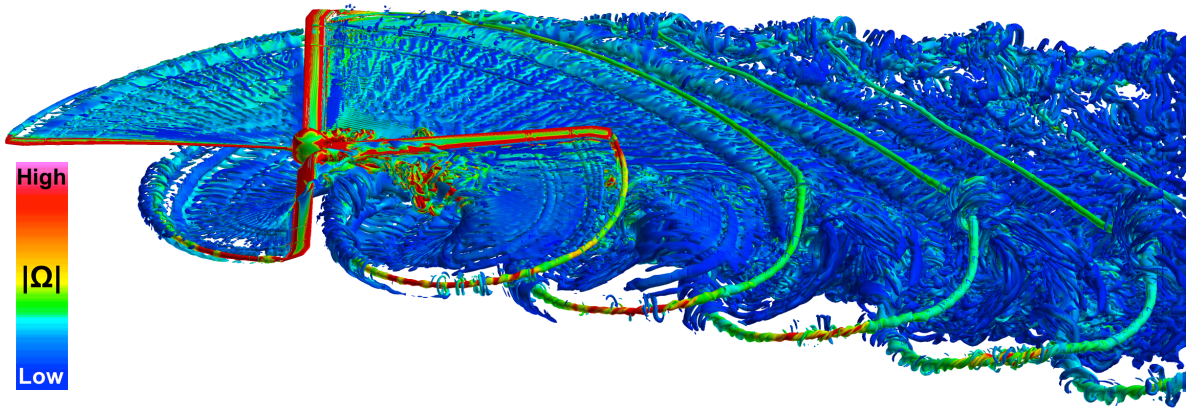

Figure 17. AMR2 vortex wake. Vortices rendered with the Q-criterion, C8534.

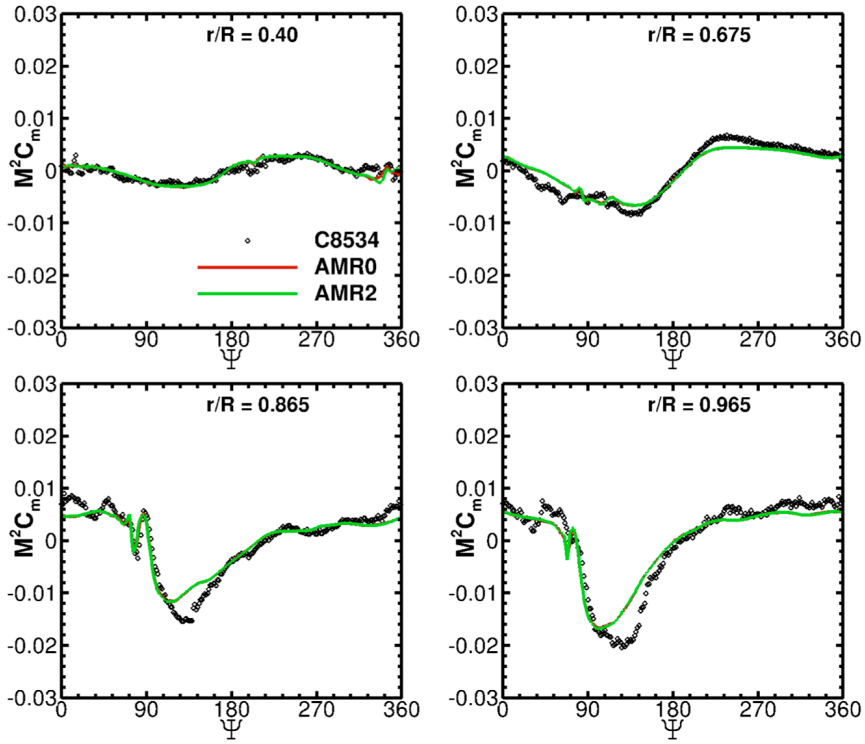

Figure 18. Pitching moment coefficient variation (mean removed) with azimuth angle at various radial stations.

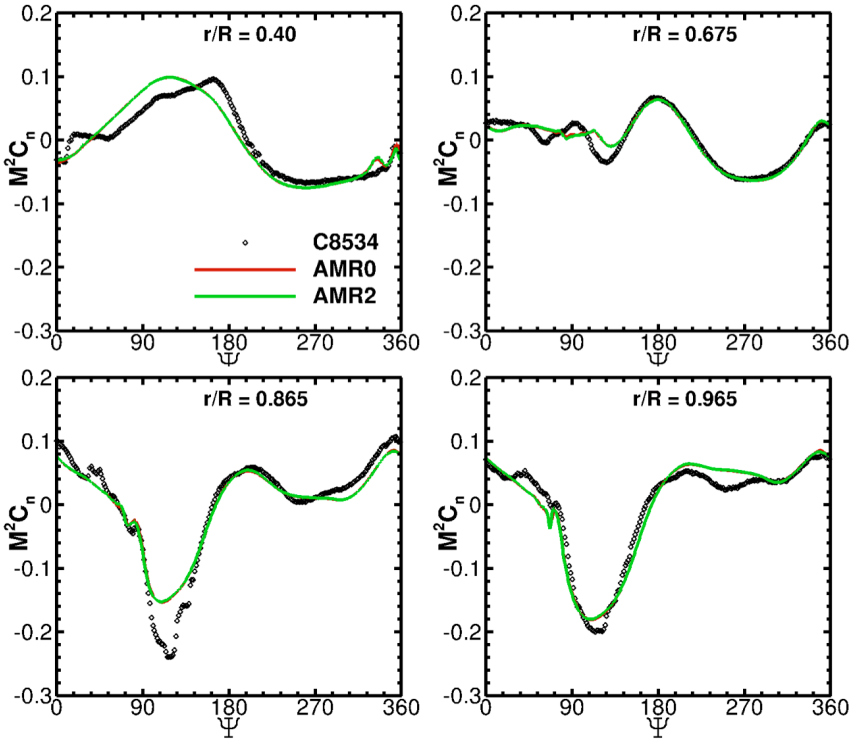

Figure 19. Normal force coefficient variation (mean removed) with azimuth angle at various radial stations.

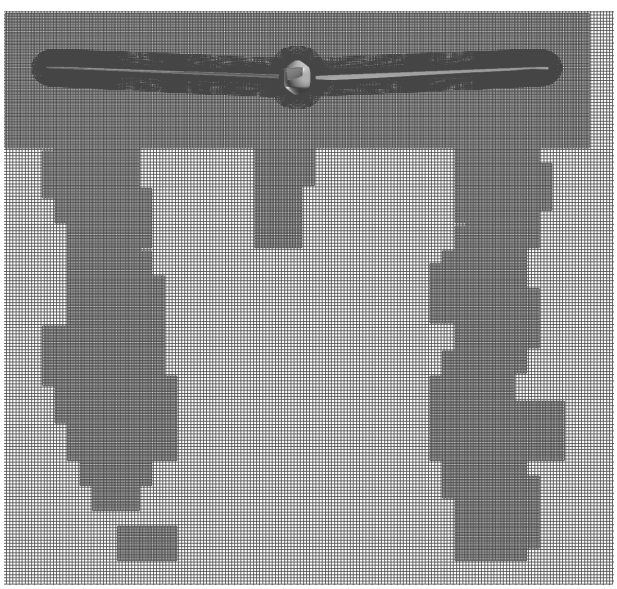

Figure 20. Baseline AMR0 grid system, Δ=10% c_{tip}, 1845 grids, 78 million grid points, hover.

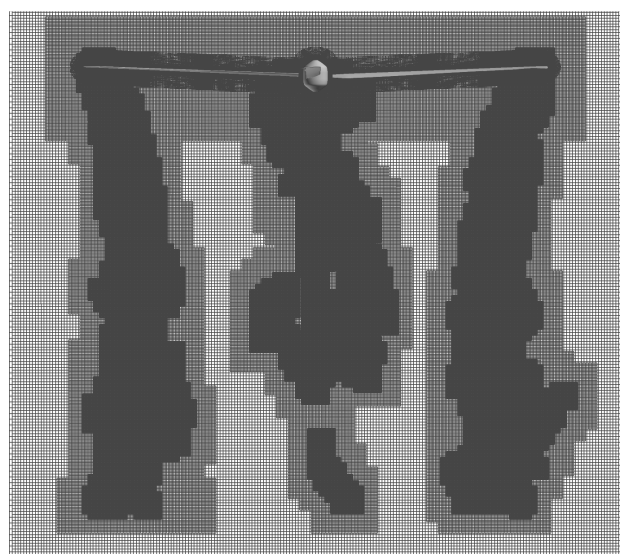

Figure 21. AMR1 grid system, Δ=10% and 5% c_{tip}, 7700 grids, 302 million grid points, hover.

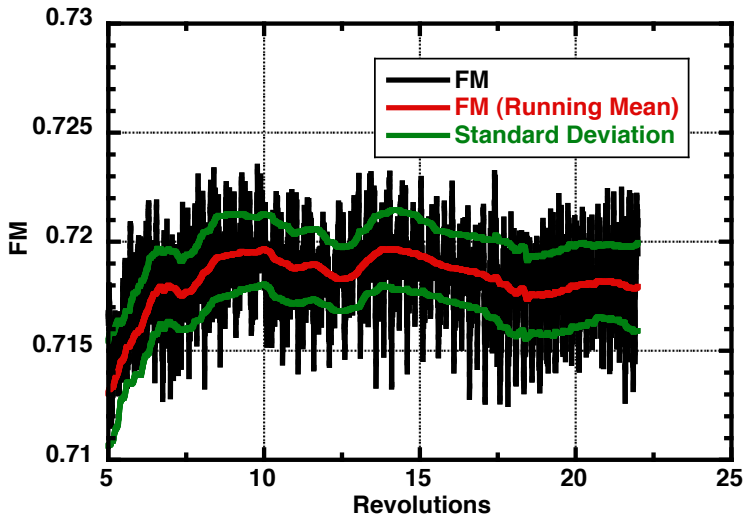

Figure 22. ARM1 FM. Grid spacing: Δ=10% and 5%c_{tip}, 7700 grids, 302 million grid points.

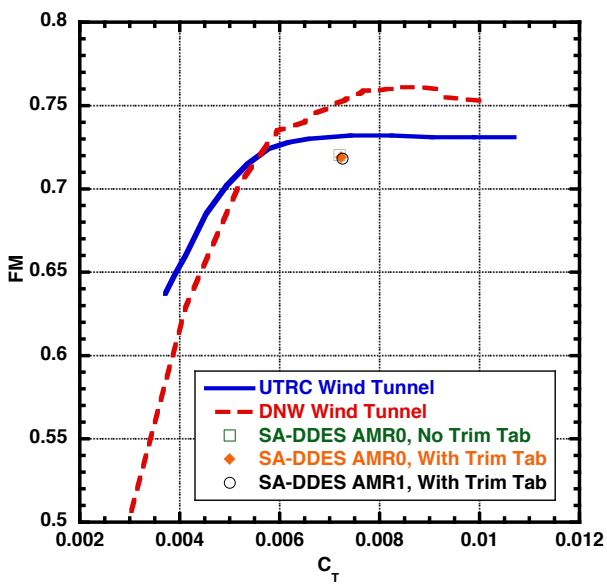

Figure 23. Comparison of OVERFLOW FM with wind-tunnel data, M_{tip}=0.238.

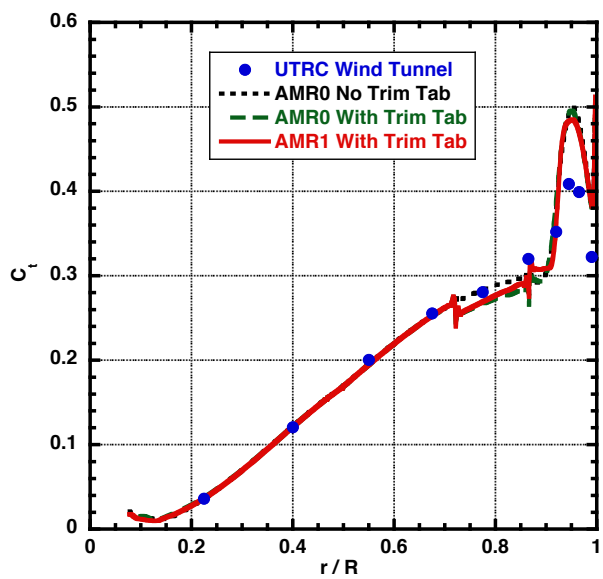

Figure 24. Comparison of OVERFLOW sectional thrust coefficient with wind-tunnel data, M_{tip}=0.238.

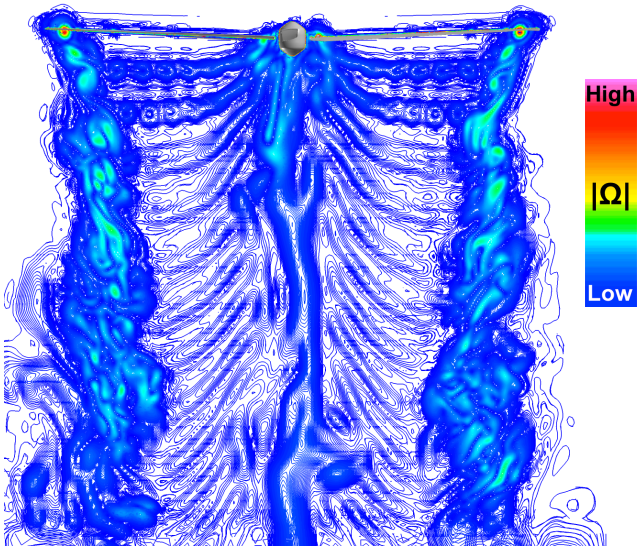

Figure 25. Vorticity magnitude contours on the y=0 plane. AMR0 tab grid system, Δ=10% c_{tip}, hover.

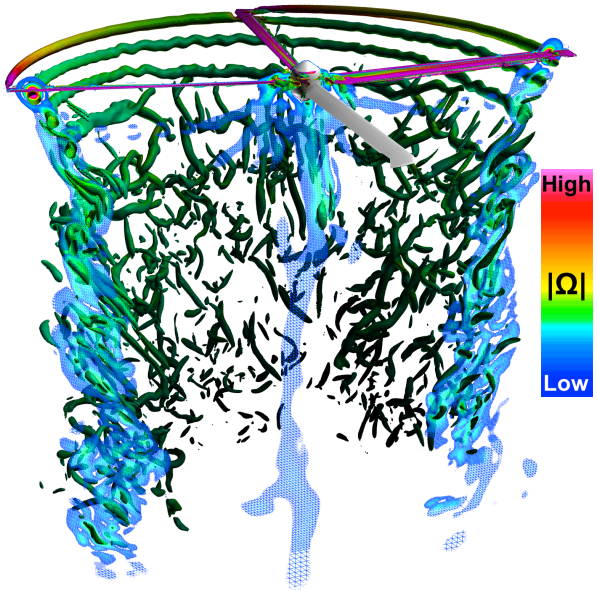

Figure 27. Cut-away view of vortex wake using the Q-criterion. AMR0 tab grid system, Δ=10% c_{tip}, hover.

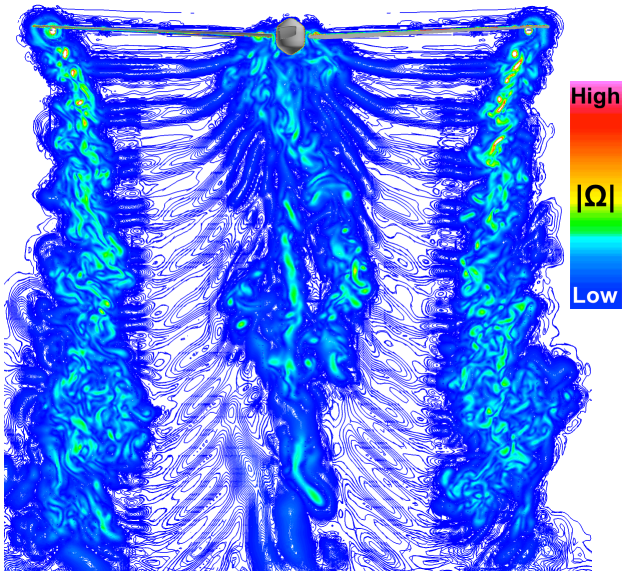

Figure 26. Vorticity magnitude contours on the y=0 plane. AMR1 tab grid system, Δ=10% and 5% c_{tip}, hover.

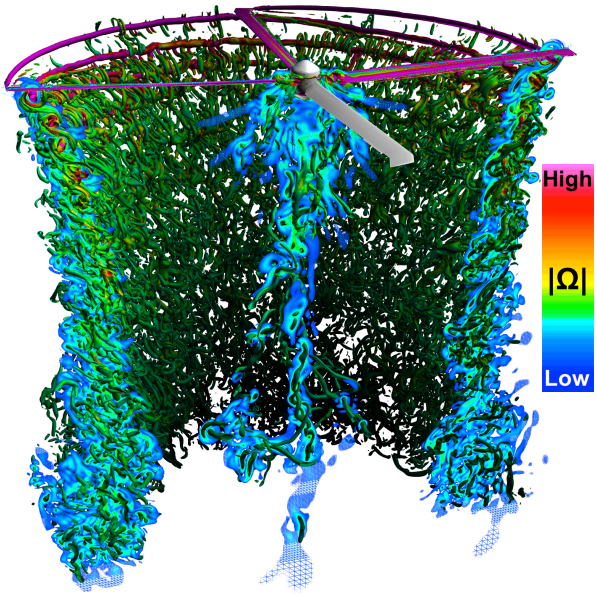

Figure 28. Cut-away view of vortex wake using the Q-criterion. AMR1 tab grid system, Δ=10% and 5% c_{tip}, hover.